Research Papers

Design and development of auxiliary energy storage for battery hybrid electric vehicle☆

Aree Wangsupphaphol [a,b], Nik Rumzi Nik Idris [a], Awang Jusoh [a], Nik Din Muhamad [a], Surachai Chaitusaney [b,*]

[a] *UTM-PROTON Future Drives Laboratory, School of Electrical Engineering, Universiti Teknologi Malaysia, 81310 UTM Skudai, Johor Darul Takzim, Malaysia*
[b] *Department of Electrical Engineering, Chulalongkorn University, Pathumwan, Bangkok 10330, Thailand*

A B S T R A C T

This paper presents a design of capacity of supercapacitor and current control for a real-scale battery hybrid electric vehicle using an acceleration and deceleration scheme. In the MATLAB/SIMULINK model, the supercapacitor current control strategy is explained and implemented. The proposed strategies' performances are evaluated by running simulations with the Extra Urban Driving Cycle and the Urban Dynamometer Driving Schedule driving cycles to examine speed tracking performance, supercapacitor current control performance, battery voltage variation, power, and energy consumption. When compared to a full-scale battery electric vehicle, the advantages are highlighted. The viability and feasibility of the proposed control strategies are then validated using a small-scale simulation and experiment. The results show that the vehicle's applicability under deceleration-based design contributes the lowest battery energy- and power consumption and voltage variation of the battery against the other schemes.

1. Introduction

Over the next decades, zero-emission vehicles like battery electric vehicles (BEVs) will replace internal combustion engine vehicles (ICEVs) and hybrid electric vehicles (HEVs) [1]. Despite the possibility of deploying BEV as the primary vehicle, the lithium-ion battery (LB) in BEV has some drawbacks, such as poor regenerative braking energy capture and short life due to lithium plating caused by highly repetitive power fluctuations [2]. Based on our experience with BEV development, the LB specification allows for a maximum discharge current of up to 7.5 times the standard charging current (C), but it is recommended that a regenerative braking current of about 1C be received. As a result, it has the potential to increase the battery life and driving range of a BEV, for example, by buffering the pulsing power [1].

To improve BEV performance, many researchers have studied the hybrid energy storage system (HESS) and the energy management system. The advantages of the HESS between LB and supercapacitor (SC) as found in recent studies are power and energy availability, battery life extension, lower battery temperature, lower energy loss, safety, and economical implementation [2]. It has varieties of HESS connections along with its control strategies. In this study, a bi-directional DC-DC converter connected to SC to parallel with the battery is deployed because of the advantages in weight, losses, cost, and reliability for battery hybrid electric vehicle (BHEV), BEV powered by HESS, application [3,4]. Regarding the control strategy for SC, the optimization-based or heuristic rule-based control strategy remains an open-ended question [5]. Optimization-based strategy requires a high-performance processor for the real-time optimal solution [6]. Nevertheless, the heuristic-based control is a good candidate for real-time implementation while the optimum solutions are not guaranteed [7]. The major problem of the heuristic rule-based control strategy for SC as presented in the literature so far is the proper real-time evaluation of the reference SC current. A disproportionate reference leads to the depletion of the SC energy before the end of the acceleration period, on the other hand, the SC cannot save the whole braking energy because of an underprivileged reference current [8].

In [8], the references for the voltage and power have been developed using the energy conservation law and the fundamental *v-i* relation of a

capacitor respectively. The reference current was derived by dividing the reference power by the SC voltage. This requires a complex control structure development with a high-performance processor. Another rule-based control strategy has been proposed in [9]. The SC charge reference was produced using a charge-speed graph, and the SC current was controlled through the current gain bandwidth. Since the SC charge was influenced by the real-time battery state-of-charge (SOC), therefore, the stored energy in the SC is not perfectly utilized. Moreover, the inner current control loop influenced by the current bandwidth can result in the current fluctuations. The study claimed that the energy is enough for acceleration but, the SC size calculation was not presented. In [10,11], the power and current of battery and SC have been separately controlled by either optimal or fuzzy adaptive control strategies. The study showed the good performance of optimal over the fuzzy control. However, the complicated structure could load the processor in a real-world application. In addition, the experiment verification has not been confirmed its viability. Conversely, a lesser complicated yet effective, the studies as in [1] proposed a rule-based control strategy to control the voltage and current of SC instead of the energy and power. The SC energy and power control can be simply controlled through a single current control obtained by the *v-i* relationship of a capacitor and the vehicle kinetic energy.

Therefore, in this paper, new heuristic rule-based control strategies referred to acceleration-based design (ABD), which is comparable to the previous study as in [1,9], and deceleration-based design (DBD) are proposed. The control strategies relate to the SC size calculations for the BHEV. The key beneficial elements of the proposed control strategies are: 1) the efficient utilization of SC in storing and releasing the energy, 2) the reduction of battery voltage variations as well as battery energy consumption, and 3) the simple implementation. In addition, our prior work was mentioned by a car manufacturer for a U.S. Patent [12], where the current finding is reported in this research.

In this paper, the effectiveness of the proposed control strategies is verified through simulations and experiments, whereby comparisons between the BEV and BHEV (with ABD and DBD) are thoroughly conducted. An actual scale simulation is performed using the actual scale of PROTON SAGA BHEV as shown in Fig. 1. Due to the constraints on the availability of the equipment and hardware, the simulation and experiment of the small-scale BHEV are performed to show the effectiveness of implementing the proposed algorithm in real-time.

The rest of the paper is presented as follows. The design of the SC based on ABD and DBD is presented in Sections 2 and 3 respectively. The contributed current control strategy of SC is demonstrated in Section 4, followed by the real-scale and the small-scale simulation/experiment in Sections 5 and 6 respectively. Lastly, the conclusion is addressed in Section 7.

2. Acceleration-based design of SC size

In ABD, the size of the SC is designed to justify the benefit of the proposed strategy in providing most of the power to assist the battery in acceleration. To find the capacitance, the vehicle kinetic energy and the stored energy in SC are balanced based on the energy conservation law. In general, the BHEV powertrain system can be separated into two parts; electrical and mechanical systems, as depicted in Fig. 1. The electrical system composes of lithium-ion batteries, SCs, DC-DC converter, motor drive system (traction inverter, and motor). The mechanical system consists of the mechanical transmission system; differential gear (DG) and driving wheels. The vehicle kinetic energy at maximum vehicle speed can be written as Eq. (1),

$$E_k = \frac{1}{2}M_V s_{V,max}^2 \tag{1}$$

where E_k is the vehicle kinetic energy, M_V is the vehicle mass and $s_{V,\,max}$ is the maximum speed of the vehicle.

The stored energy of the SC in Fig. 1 at maximum SC voltage can be calculated using Eq. (2),

$$E_{SC} = \frac{1}{2}C_{SC}V_{SC,max}^2 \tag{2}$$

where E_{SC} is the stored energy in SC, C_{SC} is the capacitance of SC and $V_{SC,\,max}$ is the maximum SC voltage, with the internal SC voltage at $t = 0$, $u_{SC}(0) = V_{SC,\,max}$.

The efficiencies of the electrical and mechanical system in Fig. 1 are used as the discharge efficiency of SC for its capacity calculation. The average efficiency of mechanical transmission (η_{mech}) and motor drive system (η_m) is obtained from the vehicle manufacturer datasheet; they are 94% in this study. The mean efficiency of SC (η_{SC}), is found from the cycle efficiency stated in the manufacturer datasheet which is between 75% and 95% [13]. One of the manufacturers claims that the efficiency in high current pulsing (positive and negative) is still over 90% [14]. Therefore, 95% is selected for SC mean efficiency optimistically. For the mean efficiency of bi-directional DC-DC converter (η_{con}), it is intentionally chosen at 97%. Thus, total efficiency for discharging the SC (η_{total}) is given by Eq. (3),

$$\eta_{total} = \eta_{mech}\eta_m\eta_{con}\eta_{SC}. \tag{3}$$

To discharge the energy stored in SC effectively, the minimum discharge voltage of SC is designated at one-half of SC terminal voltage to discharge 75% of the energy stored in SC to the tractive load effectively [15]. The energy supplied to the propulsion system is obtained by the applying of total efficiency on the energy stored in SC, as in Eq. (4),

$$\eta_{total}C_{SC-ABD}\left[V_{SC,max}^2 - \left(\frac{1}{2}V_{SC,max}\right)^2\right] = M_V s_{V,max}^2. \tag{4}$$

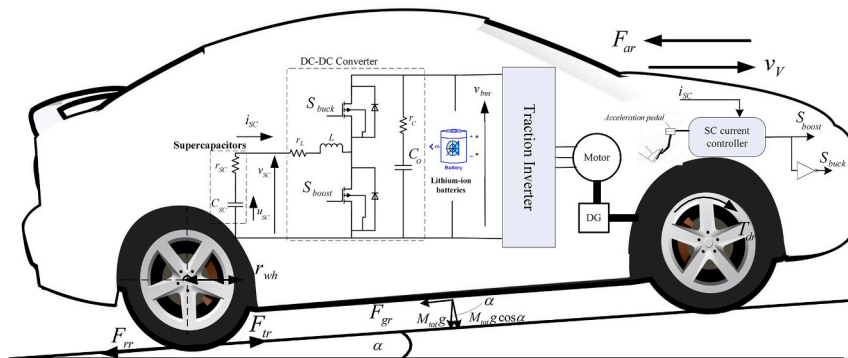As a summary, the capacity of SC for ABD, C_{SC-ABD}, can be calculated by using the equation as in Eq. (5),

Fig. 1. Schematic diagram of the proposed PROTON SAGA BHEV.

$$C_{SC-ABD} = \frac{M_V s_{V,max}^2}{\eta_{total}\left(0.75 V_{SC,max}^2\right)}. \tag{5}$$

The voltage rating of the SC is selected to match the maximum voltage gain of the boost converter. According to [8], the efficiency of the boost converter is acceptable if the maximum voltage ratio is less than or equal to 3. As shown in Fig. 1, the DC bus voltage (v_{bus}) is 260 V, thus the output voltage of SC (v_{SC}) is chosen at 200 V. It can be configured by a series/parallel connection of elementary cells or automotive modules of SC. According to Eq. (5), the SC capacity is calculated as 48 F. Therefore, the capacity of a single cell, $C_{SC, cell}$, is given by Eq. (6),

$$C_{SC,cell} = \frac{C_{SC} \cdot N_s}{N_p} \tag{6}$$

where N_s is the number of series connections ($N_s = 74$) and N_p is the number of parallel connections ($N_p = 2$).

After the capacitance of a single cell and its connection are obtained, the internal resistance of the SC bank r_{SC} can be derived from a single cell internal resistance, $r_{SC, cell}$, by Eq. (7),

$$r_{SC} = \frac{r_{SC,cell} \cdot N_s}{N_p}. \tag{7}$$

The connection of SC elementary cell 2000 F (Maxwell BCAP2000), 148 units provides the SC bank capacity for 54 F. This value is considered to approximate the calculated value, which was 48 F. The internal resistance and weight are 13 mΩ and 53 kg respectively.

3. Deceleration-based design of SC size

In DBD, SC is designed to save the regenerative braking energy instead of the battery and the result is for benchmarking with the ABD. The capacity of SC in DBD, C_{SC-DBD}, is calculated oppositely to the ABD. The energy to charge the SC is obtained by multiplying the vehicle kinetic energy with the total efficiency, as expressed by Eq. (8),

$$C_{SC-DBD}\left[V_{SC,max}^2 - \left(\frac{1}{2}V_{SC,max}\right)^2\right] = \eta_{tot} M_V s_{V,max}^2. \tag{8}$$

As a result, the capacity of SC can be calculated by Eq. (9),

$$C_{SC-DBD} = \frac{\eta_{tot} M_V s_{V,max}^2}{\left(0.75 V_{SC,max}^2\right)}. \tag{9}$$

According to Eq. (9), the SC capacity in DBD is calculated as 31 F. Thus, the capacity of a single cell can be obtained by Eq. (6) and the internal resistance of the SC bank can be derived by Eq. (7). The connection of SC elementary cell 1200 F (Maxwell BCAP1200) for 148 units provides the SC bank capacity of 32 F. This value is considered to approximate the calculated value, which was 31 F. The internal resistance and weight are 21.5 mΩ and 38.5 kg respectively.

4. Contributed control strategy of SC current

In this section, the proposed control strategies using the deterministic rule-based control strategy for controlling the SC currents for ABD and DBD are presented. The contributions of the proposed control strategies are to reduce the battery discharge power and battery energy consumption supplied to the vehicle load.

4.1. Contributed current control strategy of SC in ABD

The SC voltage reference is used for generating the current reference of SC. The simplified equivalent circuit of the SC as in [16] is used for developing the voltage control reference. By ignoring the small voltage drop across the internal resistance of SC, r_{SC}, as shown in Fig. 1, the internal voltage of SC, u_{SC}, can be simply approximated as v_{SC} [17]. According to the energy conservation law, the stored energy presented by the SC voltage can be directly related to the vehicle kinetic energy as expressed in Eq. (4). In ABD application, $\frac{1}{2}V_{SC,max}$ and $s_{V, max}$ in Eq. (4) are substituted with the time-varying internal SC voltage reference for ABD, $u_{SC, ref-ABD}(t)$, and the time-varying vehicle speed, $s_V(t)$, respectively as in Eq. (10):

$$\frac{1}{2}\eta_{tot} C_{SC}\left[V_{SC,max}^2 - u_{SC,ref-ABD}(t)^2\right] \cong \frac{1}{2}M_V s_v^2(t). \tag{10}$$

From Eq. (10), it shows the higher the vehicle speed, the lower the SC reference voltage. Thus, $u_{SC, ref-ABD}(t)$ can be obtained by Eq. (11):

$$u_{SC,ref-ABD}(t) \cong \sqrt{V_{SC,max}^2 - \frac{M_V s_V^2(t)}{\eta_{tot} C_{SC}}}. \tag{11}$$

To develop the time-varying of SC current reference for ABD $i_{SC, ref-ABD}(t)$, the *v-i* relationship of the capacitor is deployed. Therefore, the derivative of the $u_{SC, ref-ABD}(t)$ can be obtained by Eq. (12),

$$i_{SC,ref-ABD}(t) = -C_{SC}\frac{du_{SC,ref-ABD}(t)}{dt} = -C_{SC}\frac{d\sqrt{V_{SC,max}^2 - \frac{M_V s_V^2(t)}{\eta_{tot} C_{SC}}}}{dt}$$
$$= \left(\frac{M_V s_V(t)}{\eta_{tot} V_{SC,max}}\Bigg/\sqrt{1 - \frac{M_V s_V^2(t)}{\eta_{tot} C_{SC} V_{SC,max}^2}}\right)\cdot\frac{ds_V(t)}{dt}. \tag{12}$$

From Eq. (12), the SC current reference in ABD is proportional to the speed and acceleration of the vehicle; the high acceleration causes the high current reference (high power injection to the load). On the other hand, in case of no acceleration, the current reference is zero (no power injection to the load). This relation describes the intuitively dynamic behavior between vehicle acceleration and SC current. In terms of SC energy, it is inversely related to the vehicle speed as expressed in Eq. (10). The higher speed of the vehicle means the lower the reference voltage (or energy) of SC and vice versa. Therefore, the capacity of the SC is sufficient for supplying the vehicle's dynamic load.

4.2. Contributed current control strategy of SC in DBD

To control the stored energy in the SC, the energy conservation law of DBD in Eq. (8) is considered. With the same manner as in ABD, the time-varying of internal SC voltage reference for DBD, $u_{SCs, ref-DBD}(t)$, can be evaluated by Eq. (13),

$$\frac{1}{2}C_{SC}\left[V_{SC,max}^2 - u_{SC,ref-DBD}(t)^2\right] \cong \frac{1}{2}\eta_{tot} M_V s_V^2(t). \tag{13}$$

Therefore, $u_{SC, ref-DBD}(t)$ can be obtained as follows:

$$u_{SC,ref-DBD}(t) \cong \sqrt{V_{SC,max}^2 - \frac{\eta_{tot} M_V s_V^2(t)}{C_{SC}}}. \tag{14}$$

To derive the SC current reference for the current control loop, similar to ABD, the time-varying SC current reference in DBD, $i_{SC, ref-DBD}(t)$, can be derived as in Eq. (15),

$$i_{SC,ref-DBD}(t) = -C_{SC}\frac{du_{SC,ref-DBD}(t)}{dt} = -C_{SC}\frac{d\sqrt{V_{SC,max}^2 - \frac{\eta_{tot}M_V s_V^2(t)}{C_{SC}}}}{dt} \quad i_{SC,ref-DBD}(t) = -C_{SC}\frac{du_{SC,ref-DBD}(t)}{dt}$$

$$= \left(\frac{\eta_{tot}M_V s_V(t)}{V_{SCs,max}} \Big/ \sqrt{1 - \left(\frac{\eta_{tot}M_V s_V^2(t)}{C_{SC}V_{SC,max}^2}\right)}\right) \cdot \frac{ds_V(t)}{dt}. \tag{15}$$

From Eq. (15), it indicates that the SC current reference for DBD is proportional to the speed and deceleration of the vehicle as prospected in ABD. The changing speed over time generates the SC current reference. Differ from the current reference of ABD in Eq. (12), the total efficiency is displaced. Therefore, this study justifies a strategy beneficial to the vehicle application.

4.3. Current control loop of SC

The SC current references for both ABD and DBD can be developed using the closed-loop current control as shown in Fig. 2.

To design a PI-controller (PI), a small signal model of the system has to be established. In this work, a state-space averaging method is used to find the averaged state (non-linear) equations, then the average state equations are linearized to obtain the small-signal state equations [18]. Once the small-signal model is obtained, the controller is designed using the PID tuner in MATLAB. The system is analyzed with the help of Bode plots.

4.4. Small-signal modeling of Bi-directional DC-DC converter

From the schematic diagram of a bi-directional DC-DC converter in Fig. 1. The converter works in two operation modes: boost, and buck modes. The upper switch (buck switch, S_{buck}) and lower switch (boost switch, S_{boost}) are fed with switching signal with duty ratios $d(t)$ and $1 - d(t)$ respectively. In boost operation mode, the power from SC is supplied to the load, while the power from the load is recharged to SC in buck operation mode. Because the converter works complementarily, the dynamic model of the boost converter in continuous conduction mode (CCM) is chosen because it is more challenging to design the controller due to its Right Half Plan (RHP) zero. The state equations of the boost converter are derived from the physical state variables of the converter during the ON and OFF states. In general, the state variables are inductor currents and capacitor voltages related to the storage of energy. The derivatives of state variables are related to the system input to establish state equations of a linear system in matrix form [18].

To apply the state-space averaging method, the boost converter as shown in Fig. 3(a) is considered where $u_{SC}(t)$ is the time-varying internal voltage of SC, L is converter inductance, $i_L(t)$ is time-varying inductor
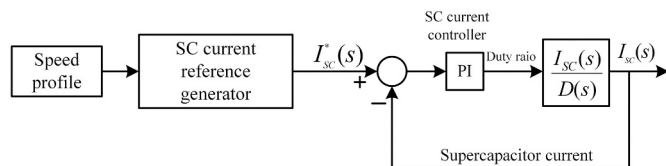
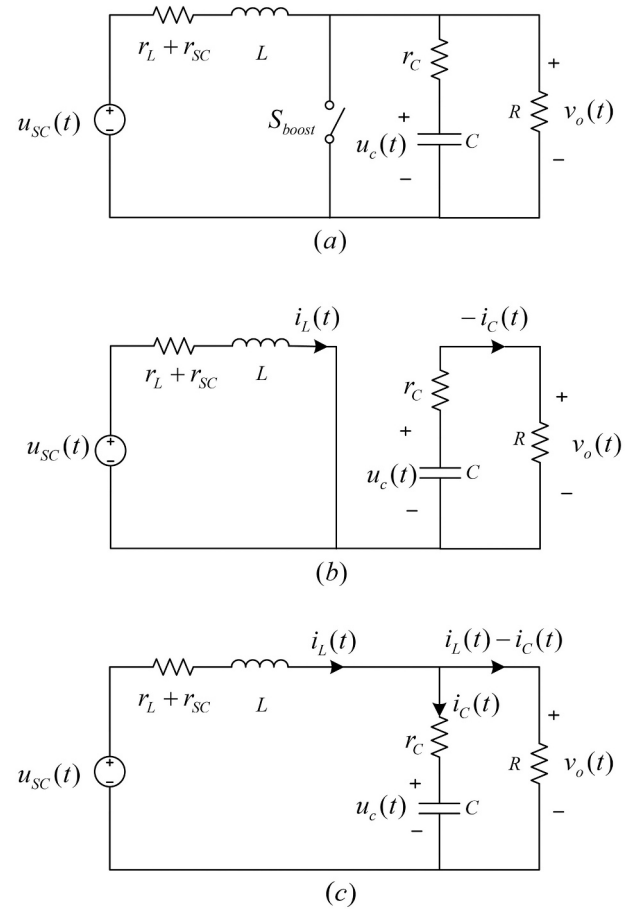**Fig. 2.** PI controller structure for SC current control.

Fig. 3. Equivalent circuit model of boost converter; (a) circuit, (b) switch ON, (c) switch OFF.

current, r_L is equivalent inductive converter resistance, r_{SC} is internal SC resistance, C is output capacitance of converter, r_C is internal output capacitor resistance, $i_C(t)$ is time-varying output capacitor current, $u_C(t)$ is the time-varying internal voltage of output capacitor, R is equivalent resistance at maximum power, and $v_o(t)$ is the time-varying output voltage. During ON state, as in Fig. 3(b), the switch S_{boost} is ON, therefore, the output capacitor supplies current to the load while the inductor receives energy from SC. Applying KVL to the inductor voltage loop, the state-space form is as in Eq. (16),

$$\frac{d}{dt}\underbrace{\begin{bmatrix} i_L(t) \\ u_C(t) \end{bmatrix}}_{\dot{x}(t)} = \underbrace{\begin{bmatrix} -\dfrac{r_L + r_{SC}}{L} & 0 \\ 0 & -\dfrac{1}{C(R + r_C)} \end{bmatrix}}_{A_1} \underbrace{\begin{bmatrix} i_L(t) \\ u_C(t) \end{bmatrix}}_{x(t)} + \underbrace{\begin{bmatrix} \dfrac{1}{L} \\ 0 \end{bmatrix}}_{B_1} \underbrace{u_{SC}(t)}_{u(t)} \quad \underbrace{i_{SC}(t)}_{y(t)} = \underbrace{\begin{bmatrix} 1 & 0 \end{bmatrix}}_{C_1} \underbrace{\begin{bmatrix} i_L(t) \\ u_C(t) \end{bmatrix}}_{x(t)} \tag{16}$$

where $\dot{x}(t)$ is the derivative of state-variable vector, $x(t)$ is the state-variable vector, $u(t)$ is the input vector, $y(t)$ is the output vector, A_1 is the state matrix during ON state, B_1 is the control matrix during ON state, C_1 is the output matrix during ON state.

From Fig. 3(c), when the switch S_{boost} is OFF, the inductor current flows to the load and output capacitor. If $R \gg r_L \cdot r_{SC}$, then $r_L \cdot r_{SC}$ can be ignored. Applying KVL, the state-space form can be written as in Eq. (17),

SC current in DBD (similar to ABD), is as in Eq. (21),

$$\frac{I_{SC}(s)}{D(s)} = \frac{1,247,231.3787\, s + 808,657,406.3969}{s^2 + 609.7559\, s + 1,595,134.7125}. \tag{21}$$

Then, the PID controller block in MATLAB/SIMULINK/Continuous is used as the controller. As the bandwidth and phase margin are designated as 1 kHz (6280 rad/s) and 75 degrees respectively, the parameter of PI, bode plot, phase margin, and gain margin of the open-loop

$$\frac{d}{dt}\underbrace{\begin{bmatrix} i_L(t) \\ u_C(t) \end{bmatrix}}_{\dot{x}(t)} = \underbrace{\begin{bmatrix} -\dfrac{(R(r_C + r_L + r_{SC}))}{L(R + r_C)} & \dfrac{-R}{L(R + r_C)} \\ \dfrac{R}{C(R + r_C)} & \dfrac{-1}{C(R + r_C)} \end{bmatrix}}_{A_2} \underbrace{\begin{bmatrix} i_L(t) \\ u_C(t) \end{bmatrix}}_{x(t)} + \underbrace{\begin{bmatrix} \dfrac{1}{L} \\ 0 \end{bmatrix}}_{B_2} \underbrace{u_{SC}(t)}_{u(t)} \quad \underbrace{i_{SC}(t)}_{y(t)} = \underbrace{\begin{bmatrix} 1 & 0 \end{bmatrix}}_{C_2} \underbrace{\begin{bmatrix} i_L(t) \\ u_C(t) \end{bmatrix}}_{x(t)} \tag{17}$$

where A_2 is the state matrix during OFF state, B_2 is the control matrix during OFF state, C_2 is the output matrix during OFF state.

To build a small-signal model at a quiescent operating point, the average description of the circuit over a switching period is derived and the results are obtained by Eq. (18),

$$\dot{x}(t) = [A_1 d(t) + A_2 \acute{d}(t)]x(t) + [B_1 d + B_2 \acute{d}(t)]u(t)$$
$$y(t) = [C_1 d(t) + C_2 \acute{d}(t)]x(t) \tag{18}$$

where $d(t)$ is duty ratio of converter and $\acute{d}(t) = 1 - d(t)$, the complement of duty ratio.

To obtain the small-signal transfer function of duty ratio to SC current, the linearized small-signal equations are transformed to s-domain using Laplace transformation as shown in Eq. (19),

$$\frac{I_{SC}(s)}{D(s)} = C(sI - A)^{-1}[(A_1 - A_2)X + (B_1 - B_2)U] + (C_1 - C_2)X \tag{19}$$

where $I_{SC}(s)$ is the SC current in s-domain, $D(s)$ is the duty ratio in s-domain, $A = A_1 D + A_2(1 - D)$, $C = C_1 D + C_2(1 - D)$, D, U and X is DC quiescent quantities of the duty ratio vector, input vector, and state-variable vector respectively.

From Eq. (19), it can be transformed to the standard equation of MATLAB transient response analysis, as given by Eq. (20),

$$\frac{I_{SC}(s)}{D(s)} = C_s(sI - A_s)^{-1}B_s + E_s; \begin{cases} A_s = A \\ B_s = (A_1 - A_2)X + (B_1 - B_2)U \\ C_s = C, E_s = (C_1 - C_2)X \end{cases} \tag{20}$$

where A_s, B_s, C_s and E_s are matrices.

Consequently, the small-signal transfer function of the duty ratio to

response of the tuned current control loop are tabulated in Table 1.

5. Real-scale vehicle simulation

5.1. Modeling of vehicle

In this paper, the performance of the vehicle is mathematically modeled in the longitudinal forces' direction. Fig. 1 shows all the longitudinal forces acting on a vehicle. Based on Newton's second law of motion, the dynamic force upon the vehicle, F_{dy}, can be described by Eq. (22) [19]:

$$F_{dy} = \sum F_{te} - \sum F_{tr} = M_V \frac{ds_V}{dt} \tag{22}$$

where $\sum F_{te}$ is the summation tractive effort and $\sum F_{tr}$ is the summation tractive resistance force, M_V is the vehicle mass in kg, and s_V is the vehicle speed in m/s.

Based on the principles of the mechanics and aerodynamics of the vehicle, the summation tractive resistance forces opposing its movement are composed of rolling resistance force F_{rr}, aerodynamic resistance force, F_{ar}, and grading resistance force F_{gr}, given by Eq. (23),

$$\sum F_{tr} = F_{rr} + F_{ar} + F_{gr}. \tag{23}$$

Rolling resistance force existed due to the tire flattening at the contact surface of the road. The rolling resistance is almost constant, and it is proportional to the vehicle mass and cosine of road slope angle, α. The main control factor is the rolling resistance coefficient, μ_{rr}, which depends on the tire characteristics. In this study, $\mu_{rr} = 0.005$ is specified based on the BEV characteristics. The calculation is given by Eq. (24),

$$F_{rr} = \mu_{rr} M_V g \cos\alpha. \tag{24}$$

Aerodynamic resistance force is the viscous resistance that drags the vehicle's body moving through the air. The constants which are used in the calculation of the aerodynamic resistance are: air density $\rho = 1.25$ kg/m^3, aerodynamic drag coefficient $C_d = 0.358$ and vehicle frontal area $A_f = 2.098$ m^2. The calculation for aerodynamic resistance is given by

Table 1
PI parameters of the current controller for SC.

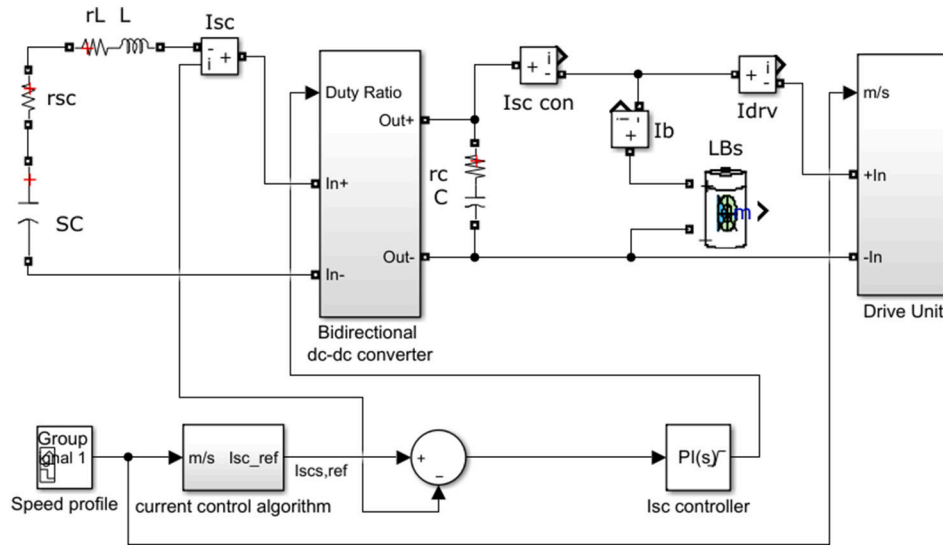| Description	Bandwidth	Phase margin	k_p	k_i
Current controller	6.28×10^3 rad/s	>60°	0.004	5

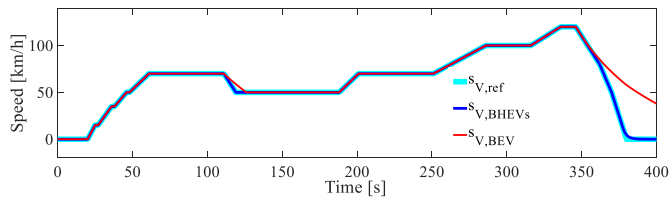**Fig. 4.** MATLAB/SIMULINK block diagram for real-scale simulation of BHEVs.

Fig. 5. Vehicle speed profiles in EUDC simulation.

Eq. (25),

$$F_{ar} = 0.5\rho A_f C_d s_V^2.$$ (25)

The grading resistance force of the vehicle can be either climbing uphill or downhill forces. The grading force is the component of the vehicle mass acting parallel to the road as given by:

$$F_{gr} = M_V g \sin\alpha.$$ (26)

In the translational simulation, the equivalent load torque is transferred to the motor's shaft, T_{eq}, is derived by considering power at the motor shaft and the moving vehicle with the mechanical transmission loss as given by Eq. (27) [20],

Fig. 6. Reference and actual current of SC in EUDC simulation: (a) BHEV-ABD, and (b) BHEV-DBD.

$$T_{eq} = \frac{F_{tr}}{\eta_{mech}} \left(\frac{s_{V,max}}{\omega_{m,max}} \right).$$ (27)

To calculate the equivalent moment of inertia referred to the motor shaft, J_{eq}, the transmission loss is neglected. Thus, the kinetic energy due to J_{eq} is the summation of the kinetic energy of various moving parts [20]. The calculation of J_{eq} is given by Eq. (28), where J_m is the moment of inertia of the motor,

$$\frac{1}{2} J_{eq}\omega_{m,max}^2 = \frac{1}{2} J_m \omega_{m,max}^2 + \frac{1}{2} M_V s_{V,max}^2$$

$$J_{eq} = J_m + M_V \left(\frac{s_{V,max}}{\omega_{m,max}} \right)^2.$$ (28)

Thus, the driving power of the vehicle can be applied for sizing the motor drive system and obtained by,

$$\omega_m T_{dr} = \omega_m T_{eq} + \omega_m J_{eq} \frac{d\omega_m}{dt} \Rightarrow P_{dr} = P_{tr} + P_{dy}$$ (29)

where ω_m is the angular speed of the motor, T_{dr} is the driving torque, P_{dr} is the driving power, P_{tr} is the tractive resistance power, and P_{dy} is the dynamic power, $\omega_m J_{eq} \frac{d\omega_m}{dt}$, is the change of kinetic energy stored in the vehicle.

5.2. Simulation result

In this comprehensive, real-scale simulation study, the Extra Urban Driving Cycle (EUDC) and Urban Dynamometer Driving Schedule (UDDS) - in Appendix A are applied to the BEV, BHEV-ABD, and BHEV-DBD. The parameters of the vehicle and SC in the designs are deployed in the simulation.

The Simulink block diagram for the simulation of BHEV-ABD and DBD is as shown in Fig. 4. The BHEV systems consist of a lithium-ion
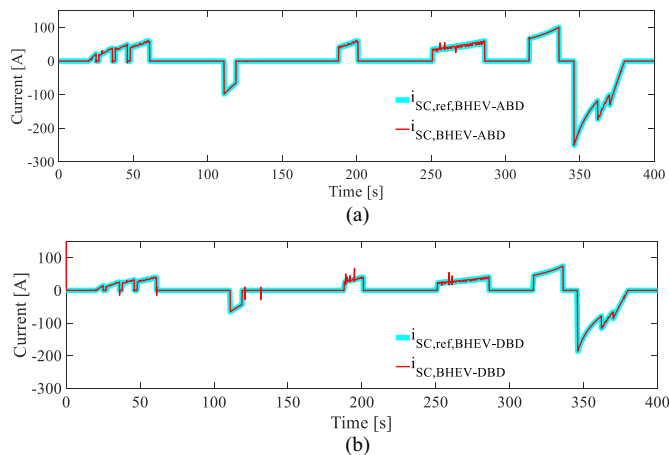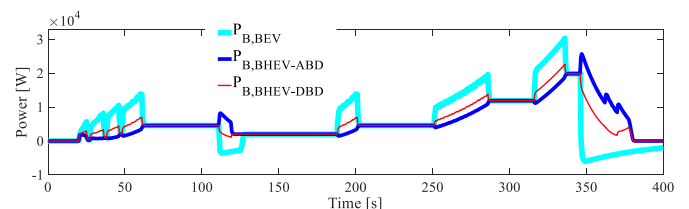

Fig. 7. Battery power of all vehicles in EUDC simulation.

battery, SC, bidirectional DC-DC converter, drive unit (with vehicle dynamic load), PI controller, and the proposed current control algorithms. For BEV simulation, the bidirectional DC-DC converter (for the SC), the controller, and SC are removed. The positive and negative current limit setting in the drive unit controller of BEV is +300 A and −30 A respectively as recommended by the manufacturer (10% of the positive current limit) to prolong the battery life, but the limits are +300 A and −300 A for BHEV.

In this analysis, a standard driving cycle, the Extra Urban Driving Cycle (EUDC), which composes of several accelerations and decelerations with a duration of up to 400 s, is used as the reference speed. The simulation result of all vehicles is shown in Fig. 5. In Fig. 5, the actual speeds of BHEVs exactly follow the speed reference. Conversely, the actual speed of BEV fails to follow the reference speed at two instances: at t = 110 s and t = 346 s. The reason for this is the battery charging current is set to only 10% of the maximum positive. From the simulation, the vehicle appears to be coasting and the braking is assisted by the aerodynamic drag and frictional force. In practice, of course, the mechanical braking system will be installed in the vehicle to stop or decelerate as desired, and this is the loss of energy recuperation in BEV.

In Fig. 6(a) and (b) (for BHEV-ABD and BHEV-DBD respectively), the actual SC currents are exactly following the references throughout the driving cycle. The BHEV-ABD has the maximum discharge current of 100 A at t = 330 s and the maximum charging current of −250 A at t = 346 s while for BHEV-DBD the maximum discharging and charging currents are 80 A and −195 A respectively. ABD draws a larger SC current than DBD, thus a more depleted SC charge in ABD after the acceleration. In a subsequent deceleration, it pulls more power from the battery to charge up the SC.

Next, the effectiveness of the proposed strategies in terms of battery power consumption is considered as shown in Fig. 7. In BEV, only the battery supplies power to the vehicle during accelerations, and the maximum power of about 30 kW occurred at t = 334 s at the end of the acceleration. In deceleration phases at t = 110 s and 346 s, the battery in BEV is recharged by the braking energy based on its recharged capability. The battery power of BHEV-ABD reaches the maximum value of 25.5 kW at t = 346 s, i.e. at the beginning of the deceleration phase. Instead, in BHEV-DBD, the maximum battery power of 22.7 kW occurred at the end of the acceleration phase at t = 334 s. It can be observed that the peak power in both ABD and DBD occurred at high-speed acceleration and deceleration phases. Larger battery power is drawn in DBD when accelerating because the SC current reference demand for DBD is lower compared to ABD. At every instant of acceleration, the battery power in DBD exceeds that of ABD; from Fig. 7, this happened at roughly t = 20 s, t = 185 s, t = 250 s, and t = 320 s. Though the battery power in ABD is much higher than that of DBD during deceleration, at roughly t = 110 s and t = 345 s. In contrast, more power from the SC is used during acceleration in ABD than in DBD. Yet, at the end of the cycle, the SOC of the SC for ABD and DBD are the same since their capacitances are differently designed. As a result, larger battery power is used in ABD than DBD to charge up the SC in the subsequent deceleration phase.

The battery voltage variation, $V_{B, var}$, is another factor to highlight the benefit of the proposed control strategies. $V_{B, var}$ indicates the amount of current drawn from or supplied to the battery. With low $V_{B, var}$, the inverter loss is reduced and the battery is protected from the
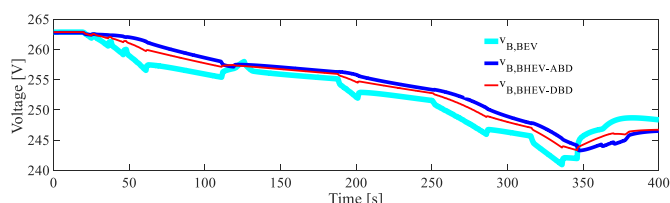
Table 2
Real-scale vehicle simulation results of EUDC.

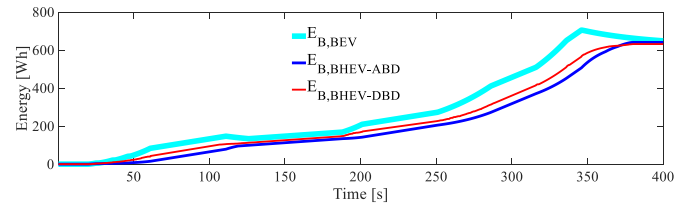|	EUDC simulation		
	$P_{B, max}$ (kW)	$V_{B, var}$ (%)	E_B (Wh)
BEV	30	8.3	649.1
BHEV-ABD	25.5	7.4	640.2
BHEV-DBD	22.7	7.3	631.5

Fig. 9. Battery energy consumption of all vehicles in EUDC simulation.
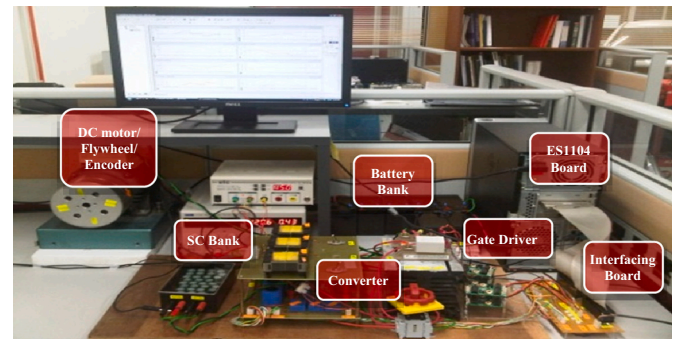

Fig. 10. The picture of small-scale propulsion hardware for experiment.

possible damaging conditions [21]. $V_{B, var}$ in all vehicles can be calculated by Eq. (30),

$$V_{B,var}(\%) = \frac{V_{B,max} - V_{B,min}}{V_{B,initial}} \cdot 100\% \qquad (30)$$

where $V_{B, max}$ is the maximum voltage of the battery, and $V_{B, min}$ is the minimum voltage of the battery.

$V_{B, var}$ for all vehicles is shown in Fig. 8. During the whole driving cycle, BHEV-DBD has the smallest voltage variation which inverses its power profile. Using Eq. (30), the voltage variation is calculated for BEV and BHEV-ABD and BHEV-DBD and tabulated in Table 2.

The battery energy consumption for all vehicles is depicted in Fig. 9. In EUDC simulation, BEV consumes the highest amount of battery energy while BHEV-DBD provides the lowest energy saving compared with BEV and BHEV-ABD by 2.7% and 1.4% respectively. The energy consumption shows in Table 2. The higher energy consumption in ABD compared to DBD is mainly due to the higher battery power which is used to charge up the SC during the deceleration phase. To sum up, DBD is the algorithm that provides the most energy-saving with significant performance to reduce battery peak power and battery voltage variation compared to other vehicles. This finding confirms with UDDS driving cycle, which is presented in Appendix A. To study the feasibility and practicability of the proposed strategies, the small-scale simulation and experiment are conducted and described in the next section.

6. Small-scale simulation and experiment

The small-scale experiment is constructed using small size battery bank manufactured by RS components Co., Ltd., model 537-5488 (80 V and 7 Ah) and a supercapacitor bank manufactured by Cooper Bussmann

Fig. 8. Battery voltage of all vehicles in EUDC simulation.

Table 3
Electric propulsion system parameters.

|		Real-scale simulation	Small-scale experiment
Battery bank			
Rated voltage	[V]	240	84
Max. cont. discharge/charge current	[A]	300/30	105/7
Capacity	[Ah]	81	7
Internal resistance	[mΩ]	57	161
SC bank			
Rated voltage	[V]	200	60
Maximum current 1 s (ABD/DBD)	[A]	(3200/2000)	N/A
Continuous current 40 °C (ABD/DBD)	[A]	(720/520)	N/A
Capacity (ABD/DBD)	[F]	(54/32)	0.83
Internal resistance (ABD/DBD)	[mΩ]	(13/21.5)	750
DC motor (separated field excited) and propulsion load			
Rated voltage	[V]	240	120
Rated current	[A]	250	3.3
Rated speed	[rpm]	1750	3000
Rated power	[kW]	60	0.187
Maximum angular velocity	[rad/s]	183.2	183.2
Equivalent moment of inertia	[kg·m^2]	34.97	0.035
Viscous friction coefficient	[N·m·s]	0.007032	0.0015
Bi-directional DC to DC converter for SC			
Inductance (ABD/DBD)	[mH]	(0.16/0.21)	5
Approximate internal resistance of inductor (ABD/DBD)	[mΩ]	(20/20)	400
Output capacitor	[mF]	1.8	10
Power IGBT module rating	[V/A]	N/A	600/100
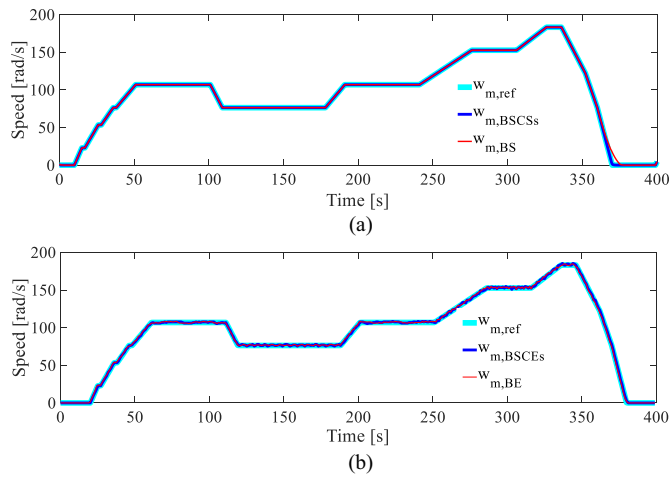
Fig. 11. Vehicle speed profiles in EUDC: (a) Simulation and (b) experiment.

Inc. (25 F in series for 30 cells) as the energy sources, and a separately excited DC motor (rated power 187 W) coupled to a mechanical flywheel where the equivalent moment of inertia of the motor and flywheel, J_m, is 0.035 kg · m^2 [3]. The DS1104 controller board is used to implement the control algorithm in real-time. The small-scale experimental set-up for the propulsion system and the corresponding hardware components is shown in Fig. 10.

In the following discussion, the small-scale simulation and experiment will be referred to the pure Battery Simulation (BS), pure Battery Experiment (BE), Battery Supercapacitor Simulation (BSCS), and Battery Supercapacitor Experiment (BSCE). The differences in the rating of the equipment, maximum speed, time scale, current limits between the small-scale and the actual-scale system in the simulation are
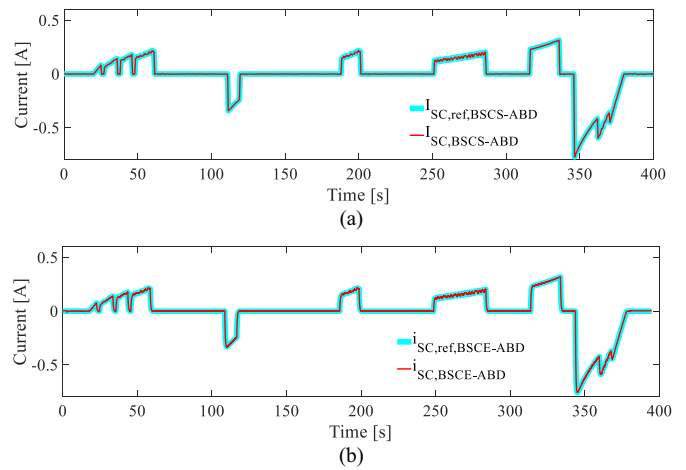
Fig. 12. Reference and actual current of SC in EUDC simulation and experiment: (a) BSCS-ABD and (b) BSCE-ABD.
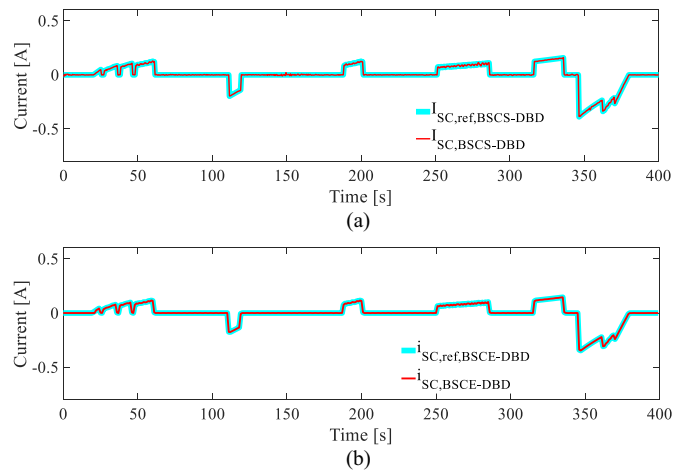
Fig. 13. Reference and actual current of SC in EUDC: (a) BSCS-DBD and (b) BSCE-DBD.
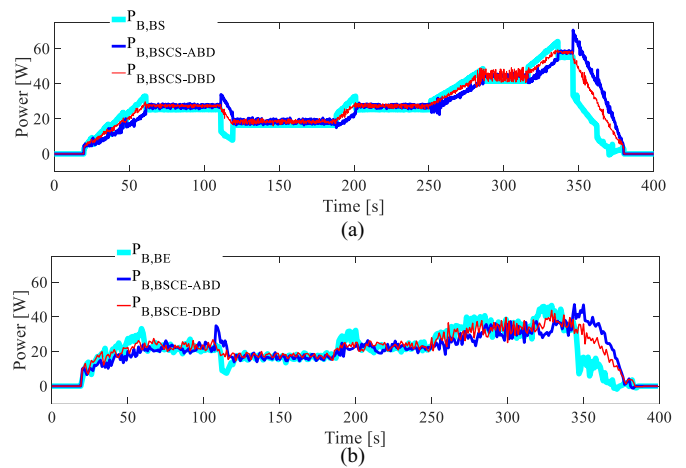
Fig. 14. Battery power profiles of EUDC: (a) Simulation and (b) experiment.

summarized in Table 3 to assist the finding hereafter.

In Extra Urban Driving Cycle Simulation and Experiment, the speed tracking performance of BS, BE, BSCSs, and BSCEs is shown in Fig. 11(a) and (b) respectively. From the figures, the actual speed exactly follows
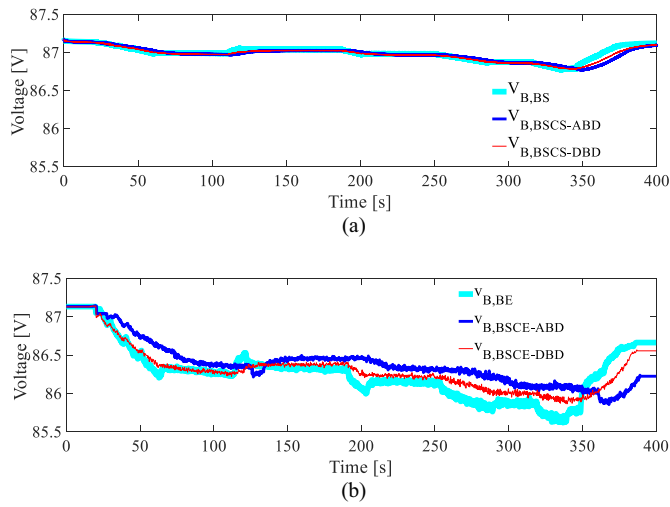
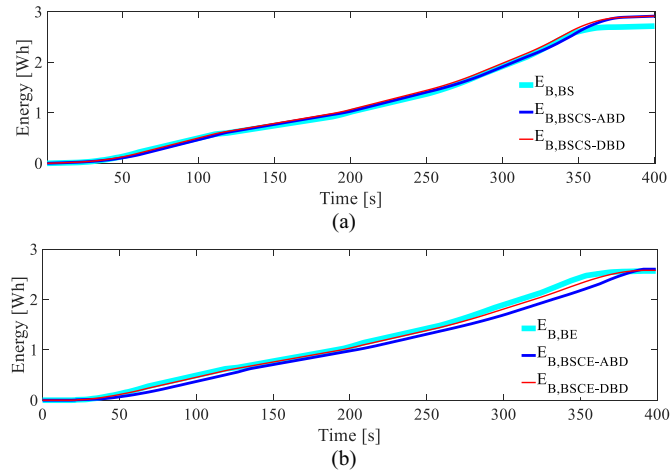**Fig. 15.** Battery voltage profiles of EUDC: (a) Simulation and (b) experiment.

Fig. 16. Battery's energy consumption of EUDC: (a) Simulation and (b) experiment.

Table 4
Small-scale experimental results of EUDC.

	EUDC experiment		
	P_B (W)	$\%V_B$ (V)	E_B (Wh)
BE	50	1.67	2.57
BSCE-ABD	51	1.45	2.60
BSCE-DBD	45	1.42	2.59

the reference speed except in BS at the last deceleration t = 367 s, the speed remaining caused by the J_m which is obtained from the average tested value. Though this has not happened in the experiment where the friction at any speed is different, thus the J_m changes.

Figs. 12 and 13 show the reference and actual SC currents for BSCSs and BSCEs. It can be seen that the actual current managed to track the reference current without any problem. Similar to the real-scale vehicle simulation, the maximum SC current is higher in ABD than DBD since higher power is fed by the SC in ABD during the acceleration compared to that of DBD. Subsequently, a higher current is drawn from the battery in ABD to recharge the SC during the braking.

The battery power consumption of BSCSs and BSCEs is shown in Fig. 14(a) and (b) respectively. Unlike the results obtained from the real-scale simulation whereby the average model is used, the waveforms

contain ripples due to the switching of the converters. From Fig. 14(a), it is found that the maximum power of all strategies occurs at 250 s < t < 350 s. The power of BSCS-ABD, BS, and BSCS-DBD is 67 W, 63 W, and 59 W respectively. In the experiment as shown in Fig. 14(b), the power has the same pattern as in simulation, and the maximum power of 51 W, 50 W, and 45 W occur in BSCE-ABD, BE, and BSCE-DBD respectively.

The simulation and experimental results of the battery voltage variation are presented in Fig. 15(a) and (b). In Fig. 15(a), the lowest voltage variation occurs in BSCS-DBD at 0.36%. BSCS-ABD and BS has voltage variation of 0.37% and 0.38% respectively. The voltage profile from the experiment as shown in Fig. 15(b) indicated that BSCE-DBD has the lowest voltage variation of 1.42%, followed by BSCE-ABD of 1.45%, and BE of 1.67%. The difference of voltage profile in simulation and experiment are from the inapplicable of battery modeling. However, their presences have the same trend.

The small-scale simulation and experiment results for battery energy consumption are shown in Fig. 16(a) and (b) respectively. It is found out that BS and BE consume energy by 2.7 Wh and 2.57 Wh respectively while the energy consumption in BSCS-ABD, DBD are 2.91 Wh, and BSCE-ABD, DBD are 2.60 Wh and 2.59 Wh respectively as in Table 4. The energy saving in experiment of BSCE-DBD compared with BSCE-ABD is by 0.4% but it is higher when compared with BE by 0.7%. Contradict to the real-scale vehicle simulation, the internal resistance of SC and converter inductor in the small-scale hardware is higher than around 20 times. Thus, the losses during the charging of the SC in the small-scale hardware are relatively higher than that of the real-scale vehicle simulation when compared to the saved energy. To justify this reasoning, small-scale simulation using real-scale vehicle parameters (SC and inductor internal resistance) is conducted and presented in Appendix B. The simulation results showed that with the small internal resistance of the SC and inductor, the results resemble that of the real-scale simulation since the losses are reduced.

7. Conclusion

This paper has presented the design of the proposed strategies; ABD and DBD. The proposed strategies are composed of two important tasks that are SC capacity calculation and control strategy development. The paper starts with the calculation of SC capacity for ABD and DBD and follows with its current control strategy development. In this paper, the performances of the proposed control strategies are investigated through real-scale vehicle simulations and small-scale simulations and experiments. The tests are carried out using EUDC. Simulation and the experimental results are in agreement thus confirms the effectiveness of the proposed strategies. These key points of the benefits of the proposed strategies are;

- The calculation of SC auxiliary energy storage for BHEV applications whereby the DBD gives the lower capacitance compared to the ABD; thus, it is lower in weight, volume, and cost.
- A novel and less complex SC current control strategy for BHEV, relative to the previously reported work as in [1], have been presented in the literature.
- The reduction in battery peak power, battery voltage variation, and battery energy consumption contributed by the DBD compared to the ABD can be observed.

Based on the simulations and experiments conducted, with the DBD strategy, the vehicle mass can be reduced, DC bus voltage becoming more stable, and the battery energy consumption is reduced thus extending the traveling range.

CRediT authorship contribution statement

Aree Wangsupphaphol: Conceptualization, Methodology development, Software, Validation, Formal analysis, Investigation, Resources, Data curation, Writing - Original draft
Nik Rumzi Nik Idris: Formal analysis, Investigation, Funding acquisition, Writing - Review & editing
**Awang Jusoh:** Formal analysis, Investigation
**Nik Din Muhamad:** Formal analysis, Investigation

Surachai Chaitusaney: Supervision, Project administration, Funding acquisition.

Declaration of competing interest

The authors declare that they have no known competing financial interests or personal relationships that could have appeared to influence the work reported in this paper.

Appendix A. Real-scale simulation of vehicles with UDDS
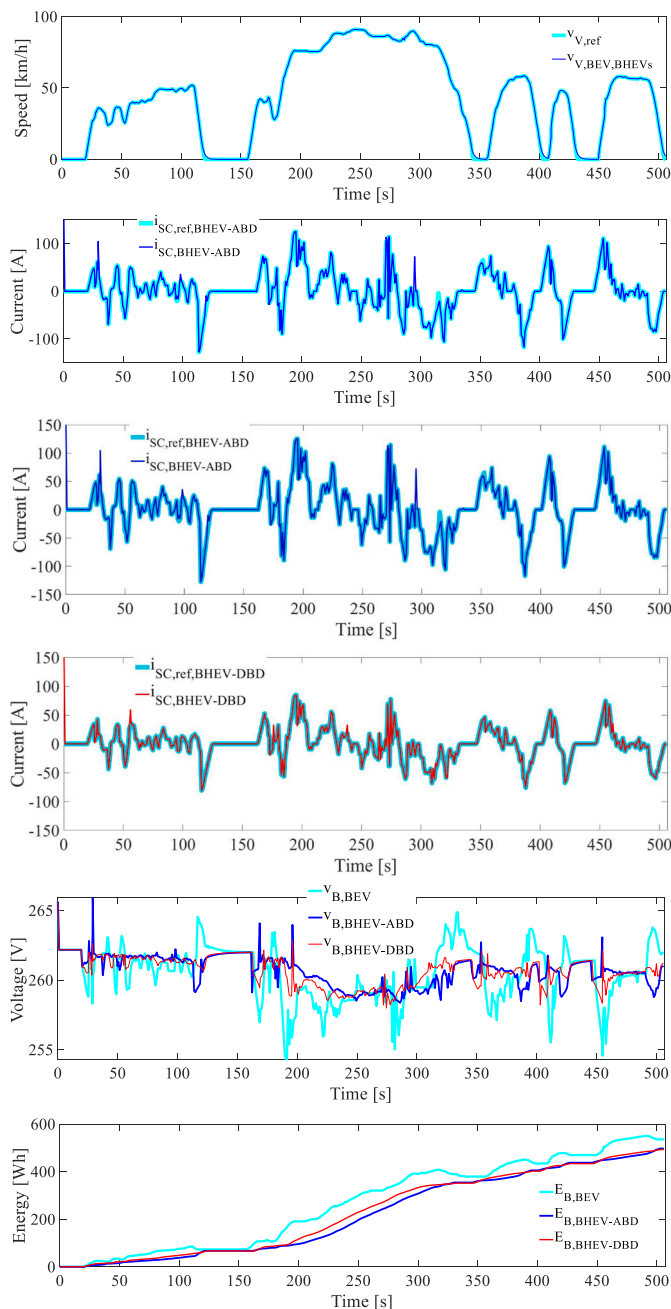
Appendix B. Small-scale simulation with maximum acceleration for battery energy consumption using the real-scale internal resistance of SC and inductor [3]
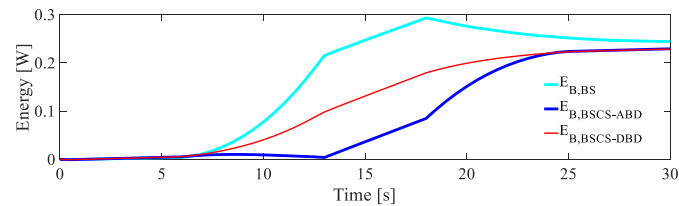
References

[1] A. Wangsupphaphol, N. Rumzi, N. Idris, Student research highlight: acceleration-based design of electric vehicle auxiliary energy source, IEEE Aerosp. Electron. Syst. Mag. (2016) 32–35, https://doi.org/10.1109/MAES.2016.140011.

[2] O. Salari, K. Hashtrudi-Zaad, A. Bakhshai, M.Z. Youssef, P. Jain, A systematic approach for the design of the digital low-pass filters for energy storage systems in EV applications, IEEEJ. Emerg. Sel. Top. Ind. Electron. 1 (2020) 67–79, https://doi.org/10.1109/jestie.2020.2999508.

[3] A. Wangsupphaphol, N. Rumzi, N. Idris, A. Jusoh, N.D. Muhamad, S. Chamchuen, Acceleration-based control strategy and design for hybrid electric vehicle auxiliary energy source, ECTI Trans. Comput. Inf. Technol. 9 (2015) 83–92.

[4] J. Huang, Z. Huang, Y. Wu, Y. Liu, H. Li, F. Jiang, J. Peng, Sizing optimization research considering mass effect of hybrid energy storage system in electric vehicles, J. Energy Storage 48 (2022), 103892, https://doi.org/10.1016/j.est.2021.103892.

[5] P. Zhang, F. Yan, C. Du, A comprehensive analysis of energy management strategies for hybrid electric vehicles based on bibliometrics, Renew. Sust. Energ. Rev. 48 (2015) 88–104. http://www.sciencedirect.com/science/article/pii/S1364032115002464.

[6] X. Lin, R. Zamora, Controls of hybrid energy storage systems in microgrids: critical review, case study and future trends, J. Energy Storage 47 (2022), 103884, https://doi.org/10.1016/j.est.2021.103884.

[7] M.F.M. Sabri, K.A. Danapalasingam, M.F. Rahmat, A review on hybrid electric vehicles architecture and energy management strategies, Renew. Sust. Energ. Rev. 53 (2016) 1433–1442, https://doi.org/10.1016/j.rser.2015.09.036.

[8] D. Iannuzzi, P. Tricoli, Speed-based state-of-charge tracking control for metro trains with onboard supercapacitors, IEEE Trans. Power Electron. 27 (2012) 2129–2140, https://doi.org/10.1109/TPEL.2011.2167633.

[9] J. Dixon, I. Nakashima, E.F. Arcos, M. Ortúzar, Electric vehicle using a combination of ultracapacitors and ZEBRA battery, IEEE Trans. Ind. Electron. 57 (2010) 943–949, https://doi.org/10.1109/TIE.2009.2027920.

[10] T. Sadeq, C.K. Wai, E. Morris, Q.A. Tarboosh, O. Aydogdu, Optimal control strategy to maximize the performance of hybrid energy storage system for electric vehicle considering topography information, IEEE Access 8 (2020) 216994–217007, https://doi.org/10.1109/ACCESS.2020.3040869.

[11] A.U. Rahman, S.S. Zehra, I. Ahmad, H. Armghan, Fuzzy supertwisting sliding mode-based energy management and control of hybrid energy storage system in electric vehicle considering fuel economy, J. Energy Storage 37 (2021), 102468, https://doi.org/10.1016/j.est.2021.102468.

[12] Y. Nissato, Clutch control device of hybrid vehicle. https://patents.google.com/patent/US8930098, 2015.

[13] U. Miller, M. John, Ted Bohn, Thomas J. Dougherty, Deshpande, Why hybridization of energy storage is essential for future hybrid, plug-in and battery electric vehicles, in: Energy Convers. Congr. Expo. 2009. ECCE 2009, IEEE, 2009, pp. 2614–2620.

[14] Maxwell Technologies, Maxwell Technologies, Inc.,White Paper—Design Considerations for Ultracapacitors, n.d. http://www.maxwell.com/images/documents/technote_designinguide.pdf.

[15] S. Member, P. Delarue, P. Le Moigne, P. Bartholomeus, The ultracapacitor-based controlled electric drives with braking and ride-through capability : overview and analysis, IEEE Trans. Ind. Electron. 58 (2011) 925–936, https://doi.org/10.1109/TIE.2010.2048838.

[16] R.L. Spyker, R.M. Nelms, Analysis of double-layer capacitors supplying constant power loads, IEEE Trans. Aerosp. Electron. Syst. 36 (2000) 1439–1443, https://doi.org/10.1109/7.892696.

[17] M. Miller, M. John, Nebrigic, Dragan, Everett, Ultracapacitor Distributed Model Equivalent Circuit for Power Electronic Circuit Simulation, Maxwell Technol. Inc, San Diego Calif., 2006.

[18] R. Erickson, D. Maksimović, Fundamentals of Power Electronics, 2004, https://doi.org/10.1007/0-306-48048-4_15.

[19] E.Mehrdad Ehsani, Yimin Gao, Ali, Modern Electric, Hybrid Electric and Fuel Cell Vehicles: Fundamentals, Theory, and Design, 2009.

[20] G.K. Dubey, Fundamentals of Electrical Drives, Alpha Science International Ltd., 2001.

[21] J. Wang, P. Liu, J. Hicks-Garner, E. Sherman, S. Soukiazian, M. Verbrugge, H. Tataria, J. Musser, P. Finamore, Cycle-life model for graphite-LiFePO4 cells, J. Power Sources 196 (2011) 3942–3948, https://doi.org/10.1016/j.jpowsour.2010.11.134.